

Laser frequency comb techniques for precise astronomical spectroscopy

Michael T. Murphy,^{1*} Clayton R. Locke,² Philip S. Light,² Andre N. Luiten,²
Jon S. Lawrence^{3,4}

¹Centre for Astrophysics and Supercomputing, Swinburne University of Technology, Hawthorn, Melbourne, Victoria 3122, Australia

²Frequency Standards and Metrology Group, School of Physics, University of Western Australia, Nedlands, WA 6009, Australia

³Australian Astronomical Observatory, Eastwood, Sydney, NSW 1710, Australia

⁴Department of Physics and Astronomy, Macquarie University, NSW 2109, Australia

Accepted 2012 January 30. Received 2012 January 4; in original form 2011 December 4

ABSTRACT

Precise astronomical spectroscopic analyses routinely assume that individual pixels in charge-coupled devices (CCDs) have uniform sensitivity to photons. Intra-pixel sensitivity (IPS) variations may already cause small systematic errors in, for example, studies of extra-solar planets via stellar radial velocities and cosmological variability in fundamental constants via quasar spectroscopy, but future experiments requiring velocity precisions approaching $\sim 1 \text{ cm s}^{-1}$ will be more strongly affected. Laser frequency combs have been shown to provide highly precise wavelength calibration for astronomical spectrographs, but here we show that they can also be used to measure IPS variations in astronomical CCDs *in situ*. We successfully tested a laser frequency comb system on the Ultra-High Resolution Facility spectrograph at the Anglo-Australian Telescope. By modelling the 2-dimensional comb signal recorded in a single CCD exposure, we find that the average IPS deviates by < 8 per cent if it is assumed to vary symmetrically about the pixel centre. We also demonstrate that series of comb exposures with absolutely known offsets between them can yield tighter constraints on symmetric IPS variations from ~ 100 pixels. We discuss measurement of asymmetric IPS variations and absolute wavelength calibration of astronomical spectrographs and CCDs using frequency combs.

Key words: instrumentation: spectrographs – instrumentation: detectors – methods: laboratory – techniques: spectroscopic

1 INTRODUCTION

A growing variety of measurements in astrophysics rely on, or are enabled by, precise astronomical spectroscopy. For example, searches for extra-solar planets via the radial velocity method (e.g. Mayor & Queloz 1995; Marcy & Butler 1996) rely on the reproducibility of stellar radial velocities over time-scales up to several years. Night-to-night reproducibility better than 1 m s^{-1} has been achieved when integrated over spectral ranges of $\sim 1000\text{--}3000\text{-\AA}$ (e.g. Lovis et al. 2006). Another example is the use of relative velocity shifts between ionic and molecular transitions in highly redshifted quasar absorption systems to constrain cosmological variations in fundamental constants, such as the fine-structure constant (e.g. Bahcall et al. 1967; Webb et al. 1999) and proton-to-electron mass ratio (e.g. Varshalovich & Levshakov 1993; Ivanchik et al. 2005). Velocity precisions averaged over several transitions in hundreds of absorption systems reach $\sim 20 \text{ m s}^{-1}$ (Murphy et al. 2003; Malec et al. 2010; King et al. 2011; Webb et al. 2011).

Much more precise and accurate spectroscopy would be required if the acceleration of the Universal expansion is to be measured by monitoring the slowly changing redshifts of Lyman- α forest absorption lines in quasar spectra (e.g. Sandage 1962; Loeb 1998). This is one possible aim of the CODEX spectrograph proposed for the European Extremely Large Telescope (e.g. Pasquini et al. 2006; Liske et al. 2008). Two epochs of spectra are required, taken decades apart, with velocity precision approaching 1 cm s^{-1} integrated over $\sim 1000\text{--}3000 \text{ \AA}$ ranges. The calibration of individual quasar exposures would therefore need to be reproducible to within $\sim 1 \text{ cm s}^{-1}$ over several decades. Many optical and mechanical elements of the telescope and spectrograph may need replacing on such a time-scale, or observations from other telescopes may need to be employed to achieve the required signal-to-noise ratio (SNR). Thus, it would be preferable to *absolutely* calibrate the wavelength scale of each quasar exposure.

Laser frequency combs (LFCs; e.g. Reichert et al. 1999; Jones et al. 2000; Udem et al. 2002) are a promising candidate for such highly precise, and possibly absolute, wavelength calibration of astronomical spectrographs (Murphy et al. 2007; Schmidt et al.

* E-mail: mmurphy@swin.edu.au (MTM)

2008). The train of pulses that are output from a frequency comb appear in frequency space as a spectrum of lines “modes” uniformly spaced by the pulse repetition rate. This repetition rate can readily be synchronised with an absolute radio frequency reference, e.g. a global positioning system (GPS) signal or atomic clock. Thus, an absolute, very dense and perfectly regular calibration spectrum could be used to calibrate astronomical spectrographs. Murphy et al. (2007) demonstrated that, in principle, recording such a frequency comb signal on a conventional charge coupled device (CCD) typical of modern astronomical spectrographs would provide enough spectral information to reach the $\sim 1 \text{ cm s}^{-1}$ calibration precision required for measuring real-time drifts in the redshifts of Lyman- α absorption lines in quasar spectra.

Prototype frequency comb calibration systems are now being tested at various observatories. The first LFC demonstration on an astronomical spectrograph by Steinmetz et al. (2008) achieved state-of-the-art calibration precision of $\sim 9 \text{ m s}^{-1}$ in near infra-red (IR, $1.5 \mu\text{m}$) astronomical spectroscopy. Wilken et al. (2010) used a frequency-doubled Yb-doped fibre laser to calibrate a single echelle order at $\sim 500 \text{ nm}$ of a highly stable vacuum spectrograph (HARPS) with 15 m s^{-1} accuracy, precision and reproducibility over several-hour time-scales. Benedick et al. (2010) calibrated the TRES spectrograph with an accuracy better than 1 m s^{-1} at $\sim 400 \text{ nm}$ using a tunable Ti:Sapphire LFC. While these tests demonstrate the main advantage of LFC calibration – the high density of high-SNR, equally-spaced modes – some challenges discussed by Murphy et al. (2007) still remain. For example, the above tests employed LFCs covering only small wavelength ranges (typically $\sim 10 \text{ nm}$). Simultaneously and uniformly illuminating the entire optical wavelength range covered by modern echelle spectrographs is highly desirable.

Another important advantage of LFC calibration is that the high density of recorded modes and the absolute frequency scale should enable direct characterization of many, if not all, instrumental systematic errors (Murphy et al. 2007). For example, in calibrating a single echelle order of HARPS, Wilken et al. (2010) found discontinuities in the calibration curve (i.e. wavelength vs. spectral pixel) at regular intervals of 512 spectral pixels. They attributed this to imperfections in CCD pixel size, shape and/or sensitivity imparted to every 512th pixel during the manufacturing process of the CCD mask. Even subtle problems in the CCD or spectrograph optics are likely to limit spectroscopic accuracy unless they are first detected, measured and then removed with LFCs.

One such problem is possible intra-pixel sensitivity (IPS) variations. Individual CCD pixels can show large spatial variations in sensitivity to photons depending on the manufacturing process and depth of the depletion layer (Toyoizumi & Ashley 2005). Pixels can also vary in size or shape and may contain small defects. Electron counts may also be registered in a pixel when a photon enters near the edge of a neighbouring one, depending on incidence angle. These, and many other effects, lead to apparent IPS variations. The development of ‘deep depletion’ CCDs has mitigated many of these effects, but even moderate IPS variations compared to those found by Toyoizumi & Ashley (2005) might affect measurements of, for example, possible variations in the fundamental constants. Thus, it is vital to accurately measure the detailed behaviour of CCD chips – even of individual pixels – if photon-limited spectroscopic precision is to be demonstrated.

This paper reports a new demonstration of an optical LFC using a very high resolution astronomical spectrograph with the aim of measuring *in situ* any IPS variations in a modern CCD. Section 2 explains our experimental setup. Section 3 sets out the basis for our

analysis to extract the IPS variations from the comb exposures. Section 4 contains our main analysis and results. Section 5 describes how series of LFC exposures might allow absolute wavelength calibration of CCDs. We summarize our main results and conclude in Section 6.

2 EXPERIMENTAL SETUP

To demonstrate that the intra-pixel sensitivity (IPS) variations in an astronomical spectrograph’s CCD can be measured *in situ*, we tested an LFC at the Anglo-Australian Telescope (AAT), Australia, on the 9th April 2010. The Ultra-High-Resolution Facility (UHRF) spectrograph has a very high resolution mode, with resolving power $R \equiv \lambda/\text{FWHM} \approx 10^6$ (where FWHM is resolution element’s full width at half maximum), which means a relatively simple LFC can be employed (Section 2.2).

Our experimental setup is illustrated in Fig. 1. After summarizing the basics of LFCs immediately below, we describe the important elements of our particular setup, including our LFC, the interface with the UHRF spectrograph and the CCD whose IPS variations we seek to measure. We also describe the data reduction steps taken before the analyses described in subsequent sections.

2.1 Laser frequency comb basics

A laser will generate light at discrete frequency modes throughout the spectral bandwidth of its gain material as long as the optical gain exceeds the losses for a full round-trip in the laser cavity at each of the mode frequencies. The frequency of a mode is determined by ensuring that there is a whole number of wavelengths in one cavity round trip. Conventionally, much effort is expended in ensuring that only a single mode can circulate at any time in the cavity; however, for mode-locked lasers, one attempts to have many modes circulating simultaneously. In addition, by including an intensity-dependent loss in the cavity it is possible to bring about a mode-locked state in which the laser’s output energy is delivered in a single, intense and temporally very short pulse. In this condition each mode maintains a fixed and well-defined phase relationship with all other modes. The frequency spacing between all pairs of adjacent modes, called the repetition frequency, is exactly the same and equal to the reciprocal of the round-trip pulse circulation time in the cavity. Further details of the operation of mode-locked lasers can be found in Cundiff & Ye (2003).

The output spectrum of the mode-locked laser appears as a comb of modes where the n th mode has a frequency, f_n , given by

$$f_n = n f_{\text{rep}} + f_{\text{CEO}}, \quad (1)$$

where n is typically of the order of 10^5 . The repetition frequency, f_{rep} , is the mode spacing between the ‘teeth’ of the comb. The carrier-envelope offset frequency (f_{CEO}) represents the offset of each mode from an exact harmonic of the repetition frequency, while in the time domain it expresses the rate at which the relative phase of the carrier and pulse envelope evolves between each pulse. For the comb to be useful as a high-precision frequency scale, f_{rep} must be stabilised and f_{CEO} should be either stabilised or monitored. The advantage of the mode-locked laser is that both f_{rep} and f_{CEO} are in the radio frequency range so they can be locked (or monitored) using relatively simple electronics. Such a comb provides a series of regular and closely spaced modes, the absolute frequencies of which are known to an accuracy limited only by that of the radio-frequency reference.

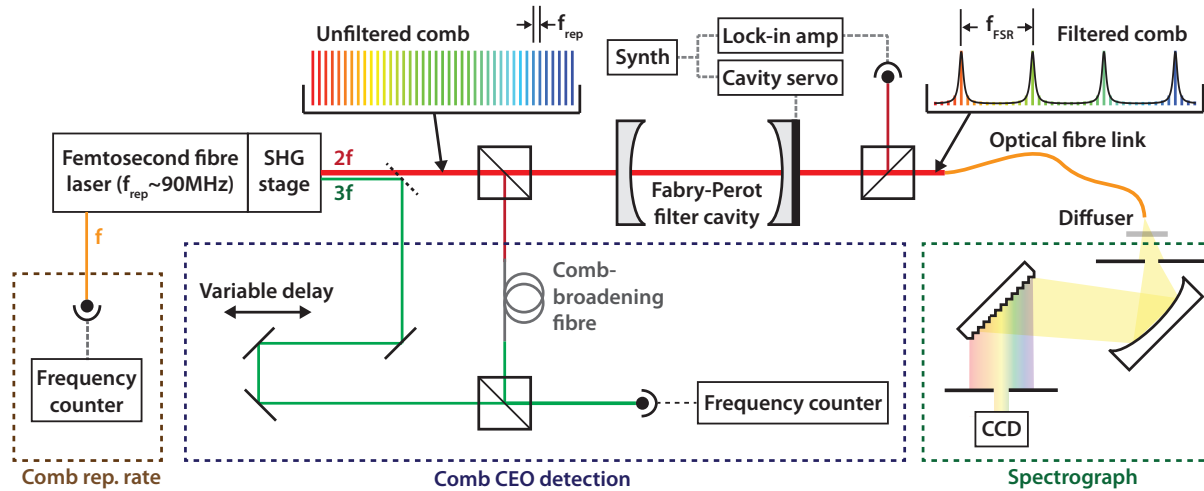


Figure 1. Laser frequency comb set-up with AAT/UHRF. The comb is fully specified by the repetition frequency, f_{rep} , and carrier envelope offset (CEO) frequency, f_{CEO} . The former is measured directly with a photo-diode and counter. The second harmonic generation (SHG) stage frequency-doubles the femtosecond-pulsed infrared laser (1.56 μm) to 780 nm ($2f$) and also produces some third harmonic light ($3f$) for the CEO measurement: the high-intensity, 780 nm light has its fairly narrow bandwidth broadened in a non-linear micro-structured crystal fibre for mixing with the 520 nm ($3f$) light. The frequency difference (‘beat note’) between them specifies the CEO frequency. Ten out of every 11 comb modes are interferometrically suppressed using a Fabry-Perot cavity, increasing the effective mode separation from 94 MHz to 1 GHz, wide enough to be resolved from each other by the UHRF in its $R \approx 940\text{ k}$ mode. The cavity’s free spectral range (FSR) is locked to the filtered comb’s effective repetition frequency by the servo electronics. The filtered comb light is transported to the UHRF pre-slit chamber where it is launched through a diffuser onto the spectrograph slit.

2.2 Laser frequency comb setup

The first frequency combs were based on solid-state Ti:Sapphire crystals (e.g. Ma et al. 2004) which, despite having exceptional frequency stability, typically require extensive supporting infrastructure and careful expert maintenance. In contrast, fibre-based mode-locked lasers are low-cost, have ‘turn-key’ operation and, importantly for demonstration at remote astronomical observatories, are portable. For these reasons we employ a commercial fibre-laser for this experiment using a stabilisation scheme developed at the University of Western Australia (Locke et al. 2009). This laser delivers a 100-fs duration pulse at 1560 nm with $f_{\text{rep}} = 94$ MHz repetition frequency at an average power of approximately 250 mW. f_{rep} was stabilised by detecting its 100th harmonic on a very fast photodiode and referencing to a stable microwave signal derived from a high quality synthesizer (see Fig. 1).

The laser output is frequency-doubled in a periodically-poled lithium niobate (PPLN) crystal, simultaneously producing a red comb with 90 mW at 780 nm together with a green comb with 200 μW at the third harmonic, 520 nm. The extraction of the offset frequency is as follows (illustrated in Fig. 1). Firstly, the green (third harmonic) comb is separated from the red (second harmonic) comb and travels a separate path on the optical table. Meanwhile, the red comb is frequency-shifted to the green wavelength (520 nm) using a unique, highly non-linear optical fibre developed at the University of Bath (Benabid et al. 2008). A delay arm in the beam path is adjusted so that femtosecond pulses from both combs arrive at an avalanche photodiode simultaneously. The difference-frequency generated by interference of the green third harmonic comb and the frequency-shifted red comb (both at 520 nm) contains the offset frequency.

Although it is possible to feed this f_{CEO} measurement back into the laser, thus actively stabilising f_{CEO} , it was not necessary for the purposes of our LFC demonstration and IPS measurement. This minimized the equipment required at the remote AAT site. Be-

cause f_{CEO} is not multiplied by n (unlike f_{rep}), it was easily logged and monitored with simple electronics during our experiments. In principle, this record could be used in post-processing to calibrate the comb, though for the purposes of our analysis in Section 4, this was not necessary.

One important characteristic of the frequency comb used here, as with all previous tests of LFCs on astronomical spectrographs, is that f_{rep} is too low for the teeth of the comb to be resolved from one another by the spectrograph (e.g. Steinmetz et al. 2008; Wilken et al. 2010). Indeed, this was one challenge for the implementation of ‘turn-key’ LFCs in astronomy discussed by Murphy et al. (2007). Our LFC’s repetition frequency, $f_{\text{rep}} = 94$ MHz, is too low even for UHRF’s highest resolution mode with $R=940000$, i.e. $\text{FWHM}=0.4$ GHz. A simple solution employed in previous works is to filter out most modes using a Fabry-Perot (FP) cavity. We chose the FP cavity’s free spectral range (FSR) to transmit only every 11th comb mode, leaving an effective mode separation of 1.03 GHz – wide enough to resolve with UHRF. In designing the FP cavity it was firstly coupled to a continuous wave laser for end mirror alignment to form a stable cavity. For it to operate with the mode-locked laser a further condition must be satisfied, that is, every 11th (in our case) pulse must map back precisely onto itself, requiring a precision in the length of the cavity of order of a few wavelengths. One of the mirrors on the FP cavity was set on a fine-screw to obtain coarse cavity length tuning, and then the optical output was monitored and used to control the cavity length via a piezoelectric transducer (PZT) on the mirror.

The dynamic range of linear response for astronomical CCDs is limited to ~ 40000 photo-electrons, the CCD studied here being no exception. Our LFC generally supplied more photons than required in short exposures; each comb exposure only needed to be a few seconds long. Therefore, individual exposures have very high SNR, dominated by the LFC photon statistics, thereby enabling constraints on the IPS variations. We are also able to test the stability of the spectrograph on short time-scales using a series of short

exposures (see Section 5.1). By comparison, the usual wavelength calibration method – a hollow-cathode ThAr emission-line lamp – provides only 3 emission lines near 780 nm which provide only moderate SNR (~ 50 per pixel) even after several minutes of exposure.

Finally, we note that our LFC setup enables a simple method for ‘flat-fielding’ (dividing out the pixel-to-pixel sensitivity variations in) the CCD exposures: we simply bypass the FP cavity to provide a high-intensity spectrum whose spectral structure is unresolved by UHRF. Again, the usual flat-field calibration method, which utilizes a quartz lamp, would have involved averaging many exposures lasting several minutes each.

2.3 UHRF spectrograph setup

The UHRF is a (grating) cross-dispersed echelle spectrograph mounted in the (east) coudé room of the AAT (Diego et al. 1995). It was selected for our LFC test because its very high resolution mode ($R=940000$) allows us to use a relatively inexpensive, commercial LFC with a ‘low’ (actually typical) f_{rep} . The demands on the finesse of the FP cavity mirrors (which was $F \sim 300$) are also reduced because ‘only’ 10 out of every 11 comb modes need to be interferometrically suppressed. And while UHRF in this mode only allows ~ 1 nm of a single echelle order to be observed in a single exposure, a wider bandwidth was not required for measuring possible IPS variations. Also, pre-defined echelle and cross-disperser angles were already available for observing at 780 nm, so minimal time was spent configuring the spectrograph itself.

The FP-filtered comb light was coupled into a single-mode optical fibre for transport to UHRF’s pre-slit chamber where it was launched in free space through a rotating paper diffuser to overfill the slit in the spectral direction and almost fill it in the spatial direction. The full UHRF resolving power of $R=940000$ was achieved by using the smallest slit-width possible, just 40 μm , or 0.059 arcseconds projected on the sky. The slit had an unvignetted length of ~ 3.4 mm, or ~ 5 arcseconds. The alignment of this simple launch setup was checked only by eye using a television camera system to view the 780 nm light falling on cards placed along UHRF’s optical axis. The laser light (almost) filled the UHRF collimator symmetrically about its centre. The alignment was not altered throughout the exposure sequences reported in this paper.

Once the optical alignment of the launch system was finalised, the CCD dewar was manually rotated around the optical axis and fixed so that UHRF’s spectral direction roughly aligned with the CCD rows. This simplified the analysis by ensuring that comb spectra from individual CCD rows spanned the entire length of the CCD.

2.4 Charge-coupled device (CCD) details

The CCD studied here, called ‘MITLL3’ at the AAT, is chip 2 from wafer 67 (i.e. device W76c2) of fabrication run CCID-20 from MIT/Lincoln Labs. It has 2048×4096 15×15 - μm pixels and was designed to have a deep depletion layer (i.e. high resistivity), yielding pixels which are effectively 40 μm thick.

Several trade-offs were considered in selecting the MITLL3 chip over another commonly-used chip at the AAT, a back-side illuminated, thinned EEV chip with 2048×4096 13.5×13.5 - μm pixels. The latter is used for precise radial velocity work at the AAT (e.g. Tinney et al. 2003) which might benefit from knowing the IPS variations in that device. Nevertheless, chips from the same

fabrication run (CCID-20) as the MITLL3 are used at many telescopes world-wide in many different instruments including, for example, the Ultraviolet and Visual Echelle Spectrograph at the Very Large Telescope, Chile (Dekker et al. 2000). Another consideration is that, being thinned and back-side illuminated, the EEV chip’s IPS variations may be larger and more easily detected by our LFC test. Conversely, IPS variations in the deep-depletion MITLL3 chip might be harder to detect.

However, the main factor in selecting the MITLL3 chip was its very low fringing level at 780 nm. The much larger fringing level of the EEV would have prevented adequate flat-fielding of our comb exposures and precluded any measurement of the IPS variations in the EEV chip.

For reference, the MITLL3 CCD pixel size in the spectral direction of 15 μm translates to 2.63 $\text{m}\text{\AA}$ or, at 780 nm, 129 MHz or 101 m s^{-1} . The nominal resolving power of $R = 940000$ at 780 nm translates to a FWHM resolution of 8.3 $\text{m}\text{\AA}$, 409 MHz or 319 m s^{-1} . The FWHM resolution is sampled by 3.15 pixels.

2.5 Data reduction

Before any analysis of IPS variations, only basic data-reduction steps were required. The bias level was estimated using the median of 51 zero-second CCD exposures and subtracted from each CCD exposure. As mentioned in Section 2.2 above, flat-field exposures were obtained by bypassing the FP cavity stage. A master flat-field, formed from the median of 31 such exposures with high photo-electron counts, was used to normalize each LFC exposure used in our analysis. Part of a bias-corrected, flat-fielded LFC exposure is shown in Fig. 2. Note that the spectrum’s spatial direction is tilted with respect to the CCD columns, a fact which assists our subsequent analysis.

It is important that the error spectrum – the flux uncertainty in each CCD pixel – is estimated for our analysis of possible IPS variations. The dominant noise source is the Poisson noise of the LFC photons; the CCD’s read-noise was only ~ 3 photo-electrons per pixel. Thus, the error spectrum varies strongly along the spectral direction of any given CCD row. An error image was generated for each bias-corrected, flat-fielded LFC exposure by taking the square root of the bias-corrected flux image and normalizing by the master flat-field image. The error spectrum is shown for a single CCD row in Fig. 2.

3 MODELLING THE FREQUENCY COMB CCD EXPOSURES

To understand the extent of IPS variations in the CCD pixels, we model the frequency comb flux using non-linear least squares χ^2 minimisation (e.g. Fisher 1958). The reliability of this technique is demonstrated using simulated comb CCD recordings where relevant in the following sections. It is possible that other techniques would be effective, perhaps even simpler or faster but, for the demonstration purposes of this paper, a full exploration of other techniques is not important. The χ^2 minimisation code is custom-written but employs the standard Levenberg–Marquardt method with an implementation following the basic structure of that set out in Press et al. (1992).

We begin by modelling the UHRF instrumental line-shape (or instrumental profile) from the 1-dimensional comb spectrum in individual rows of the comb CCD exposures (Section 3.1). That

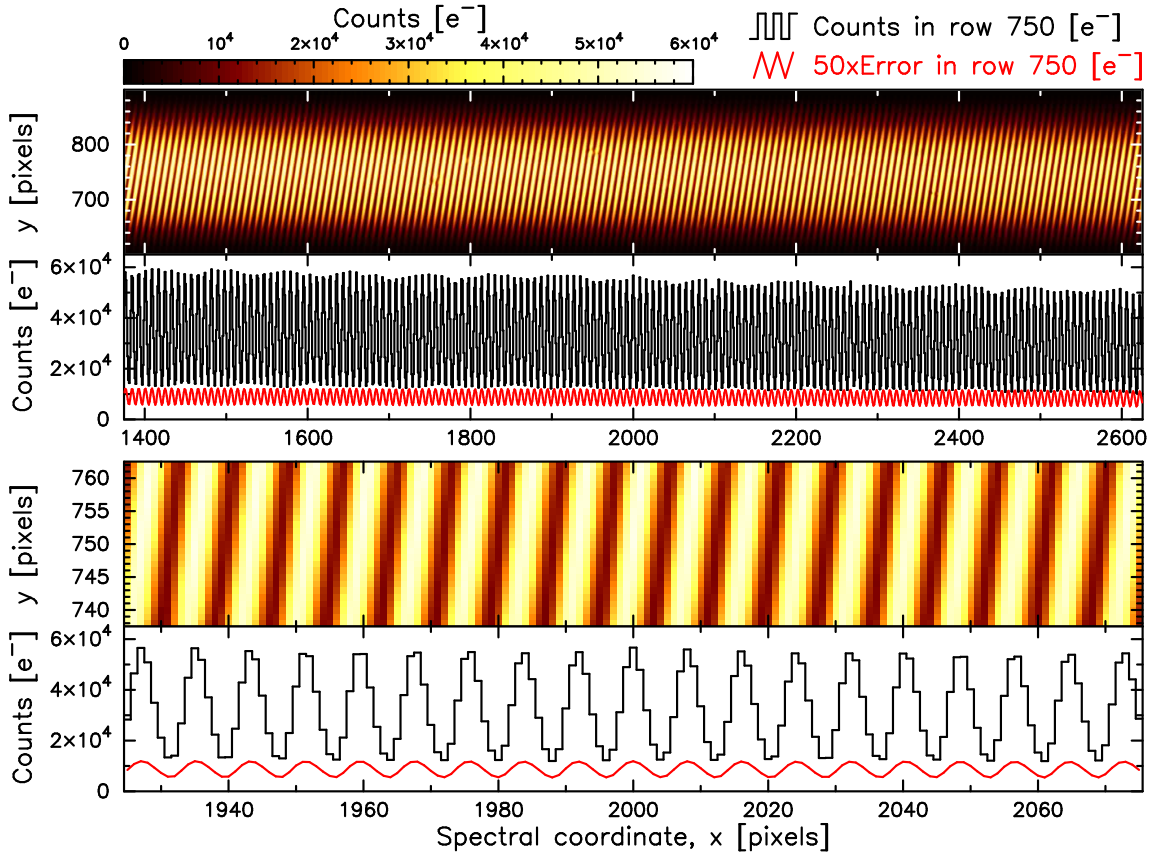


Figure 2. Part of a CCD exposure at 780 nm from the AAT/UHRF frequency comb test (top panel) and the electron count spectrum extracted from a single CCD row ($y = 750$; second panel from top, black histogram). The raw CCD image was bias-corrected and flat-fielded before plotting. The spatial direction is clearly tilted with respect to the CCD columns. The lower two panels show a zoomed-in portion of the upper two panels. The lowest panel shows a small number of the comb modes transmitted through the Fabry-Perot cavity (see Fig. 1) which have a spacing of ~ 8 pix in the spectral direction (x coordinate). Plotted below the single-row spectrum (black histogram) is the error spectrum derived from photon statistics (red line) exaggerated by a factor of 50.

model is constrained by the assumption that other observed spectrum properties (e.g. average flux, frequency dispersion per CCD pixel) vary only slowly across the CCD. This basic model of the instrumental line-shape is then fixed (though its parameters remain free) and the IPS variations are introduced to the comb model in Section 3.2.

3.1 Modelling the instrumental line-shape (ILS)

For our purposes, the instrumental line-shape (ILS) is defined as the profile formed in a single CCD row by an infinitely narrow LFC mode after passing through the spectrograph. Note that our LFC's modes are completely unresolved by UHRF and so each recorded comb mode will directly represent the ILS at its observed wavelength. The frequency stability of our LFC implies that the spectral width of each comb mode is ~ 1 MHz, or $\sim 0.8 \text{ m s}^{-1}$ at the observed wavelength of 780 nm. Given the nominal UHRF resolution of $\approx 320 \text{ m s}^{-1}$, the comb modes are very much unresolved.

For a single CCD row, we initially model the comb flux, F_i (in electron counts), in CCD pixel i as the product of an ‘envelope intensity’ function, $E(x)$, and a ‘comb function’, $C(x)$, both of which are functions of position in the spectral direction of the CCD, x :

$$F_i = \int_{i-1/2}^{i+1/2} E(x) C(x) dx \approx E_i \int_{i-1/2}^{i+1/2} C(x) dx. \quad (2)$$

The sensitivity of F_i to IPS variations is directly linked to the

fact that the comb function varies quickly on the scale of a single CCD pixel, so it is important to integrate the model of the comb across the pixel rather than approximate it by taking, e.g. its value at the pixel's centre. However, the envelope intensity of the comb, $E(x)$ – the variation in the measured peak intensity from mode to mode – varies very slowly along the spectrum; the approximation in the right-hand-side of equation (2) reflects this. For all the fits conducted in this paper, $E(x)$ is simply approximated as a second order polynomial.

Because the LFC modes are much narrower than the UHRF resolution, in equation (2) the comb function, $C(x)$, can be written as a sum of ILSs from each comb mode,

$$C(x) = \sum_{n=1}^{\infty} \text{ILS}(x, x_n). \quad (3)$$

The n th mode of the comb transmitted through the Fabry-Perot cavity occurs at pixel position x_n given by

$$x_n = x_0 + \omega_1 n + \omega_2 n^2 + \dots, \quad (4)$$

with ω_1 , the ‘pixel-space repetition frequency’. Equation (4) is analogous to equation (1) but, because we model the comb in pixel space rather than frequency space, higher-order terms are required, characterised by ω_2 , ω_3 etc. In this work we found no need to include terms beyond second order in equation (4) because we model such short frequency ranges of comb spectra. Visual inspection of Fig. 2 reveals that comb modes fall on approximately every

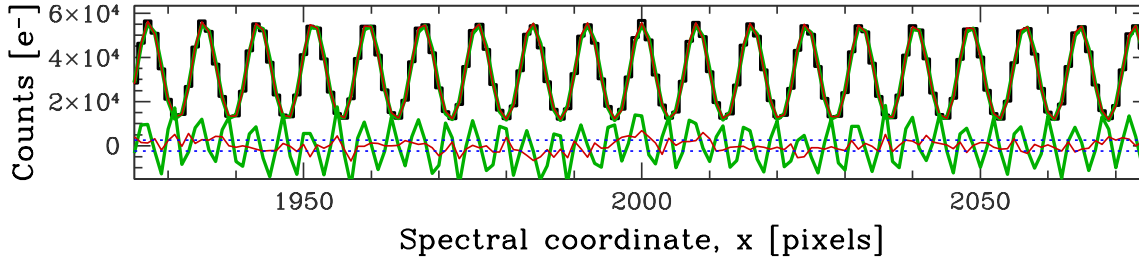


Figure 3. Modelling the instrumental line-shape (ILS) from small sections of comb spectra. The plot shows single- and double-Gaussian ILS models (thick green and narrow red lines, respectively; the latter lies almost entirely over the former) fitted to part of row $y = 750$ of a single flat-fielded comb exposure (black histogram). The residuals between the two models and the data (again, single-Gaussian in thick green, double-Gaussian in narrow red), normalized to the $1\text{-}\sigma$ errors, are plotted below the spectrum relative to the $\pm 3\text{-}\sigma$ levels (dotted blue lines). Although the two fits are almost indistinguishable by eye, the residual spectra show that the double-Gaussian ILS model is strongly preferred.

8th pixel – i.e. $\omega_r \approx 8 \text{ pix}$ – without any obvious non-linearity, i.e. $n\omega_2 \ll \omega_r$. Indeed, in our detailed modelling below, ω_2 is typically $\sim -1 \times 10^{-4}$ with $-50 \lesssim n \lesssim 50$.

Visual inspection of the example comb spectrum recorded in a single CCD row (see Fig. 2) reveals UHRF’s ILS to be slightly asymmetric. Our initial guess for the ILS was therefore a double-Gaussian model: a central Gaussian flanked by a weaker second one with the same width. That is,

$$\text{ILS}(x, x_n) = \sum_{m=1}^M A_m \exp\left[-(x - \Delta_m - x_n)^2 / 2\sigma_{\text{ILS}}^2\right] \quad (5)$$

with $M = 2$, $\Delta_1 \equiv 0$ and the ratio of Gaussian amplitudes, A_2/A_1 , normalized so that $\int_{-\infty}^{\infty} \text{ILS}(x, x_n) dx = 1$.

Figure 3 shows the model specified in equations (2–5) fitted to a small section of a single row of one comb exposure. Also plotted is the same model but with a single Gaussian ILS instead of a double-Gaussian (i.e. $M = 1$ instead of 2). The two models are not readily distinguishable by eye. However, the residual spectra clearly show that the double-Gaussian model provides a closer match to the data. This is also reflected in the values of χ^2 per degree of freedom, ν , for the two fits: $\chi_\nu^2 = 29.5$ and 2.7 for the single and double-Gaussian models respectively. We discuss why the latter value is noticeably greater than unity in Section 4.2. The residual spectrum for the double-Gaussian model, also plotted in Fig. 3, does not appear to show any features which repeat on the scale of the comb mode structure, unlike that for the single-Gaussian model. We attempted to include a third Gaussian (i.e. $M = 3$) in the ILS but its best-fitted amplitude was typically very small ($A_3/A_1 \lesssim 0.02$) and, upon fitting different CCD rows and using different CCD exposures, its separation from the main Gaussian component was sporadic and very weakly constrained. This is consistent with the lack of periodic structure in the residuals from the double-Gaussian model in Fig. 3. Also, including the third Gaussian barely reduced χ_ν^2 in most cases; when fitting some CCD rows from some exposures it actually increased. That is, there is no clear evidence for additional structure in the ILS beyond the double-Gaussian model.

Diego et al. (1995) measured the UHRF ILS using a He-Ne laser. From their figure 10, their measured ILS can be described as comprising two main Gaussian-like components separated by $\sim 0.25 \text{ km s}^{-1}$ with similar widths of $\text{FWHM} \approx 0.28 \text{ km s}^{-1}$ and with one being ≈ 20 per cent the height of the other. This accords well with the ILS model derived from the comb spectra: in the simple fits above, the Gaussian components were separated by $\approx 0.23 \text{ km s}^{-1}$, they had $\text{FWHM} \approx 0.30 \text{ km s}^{-1}$ and the weaker one was 20 per cent the height of the stronger one. Thus, the double-

Gaussian model of the UHRF ILS seems well justified, both from the comb spectra themselves and the He-Ne spectra of Diego et al. (1995).

When fitting different parts of the same CCD exposure studied in Figs. 2 & 3, and the others taken over the course of our LFC test, we found no significant variations in the ILS structure. That is, no further Gaussians seem to be required. Nor do we observe large variations in the parameters of the two Gaussians constituting our preferred ILS model; when modelling a 2-dimensional comb spectrum in Section 4 we explicitly test for this possibility. However, throughout this rest of this work we adopt the basic double-Gaussian model of the ILS with free parameters as specified in equation (5).

Finally, a by-product of the above fits is the statistical uncertainty on x_0 in equation (4), the zero-point of the comb function. For example, the double-Gaussian fit to the 150 spectral pixels in Fig. 3 returns a $1\text{-}\sigma$ uncertainty on x_0 of $9.9 \times 10^{-3} \text{ pix}$, or $\approx 1 \text{ m s}^{-1}$. In the absence of intra-pixel sensitivity variations (which we seek to measure in this work), this would correspond to the precision with which such short sections of the comb spectrum could be wavelength-calibrated.

3.2 Modelling CCD intra-pixel sensitivity (IPS) variations

In our comb test with UHRF we sought to detect or limit any IPS variations only in the spectral direction across the CCD pixels. This is possible because the flux measured in a given pixel will depend on the IPS variations most strongly when the comb flux changes substantially across a pixel. From the example comb exposure shown in Fig. 2 it is clear that the flux variations in the spatial direction are much more slowly varying compared with those in the spectral direction. Therefore, we do not attempt to model or detect IPS variations in the spatial direction across pixels.

Thus, when fitting the comb flux in a single CCD row, or part thereof, we insert a term for the IPS map, $\text{IPS}_i(x)$, in equation (2) to obtain

$$F_i \approx E_i \int_{i-1/2}^{i+1/2} C(x) \text{IPS}(x) dx, \quad (6)$$

where, as discussed above, $\text{IPS}(x)$ is the same for all i , or $\text{IPS}_i(x) = \text{IPS}(x)$.

Our aim here is to measure the average IPS variations, not the IPS map for individual pixels. The latter possibility is discussed in Section 5. We therefore make two important assumptions in the modelling that follows:

(i) The IPS variations in all CCD pixels under consideration are assumed to be the same. While previous laboratory studies have shown that IPS variations are different in different pixels, they also demonstrate a high degree of correlation across large portions of the CCD (e.g. Toyozumi & Ashley 2005).

(ii) The IPS variations are modelled as a symmetric function about the centre of the pixel (in the spectral direction). We report results here from a Gaussian function with variable width, truncated at the pixel edges and a base fixed at zero with no slope. For Gaussian widths larger than $\text{FWHM} \sim 0.5$ pixels, which we find are always preferred for the UHRF CCD, a variable base would be closely degenerate with the width parameter. Similar functions – e.g. symmetric linear slopes away from a central IPS peak (or trough) to the pixel edges – give very similar results. It is also important to realise that a variable baseline slope would be closely degenerate with the parameters in equation (4) which characterize the position of the comb modes. That is, a general slope in the IPS map of the fitted pixels is not detectable in our work. We discuss this further in Section 5.2.

We will see in Section 4.2 that it is only by fitting many hundreds of pixels (all assumed to have the same IPS map) that the degeneracies in our fitted model are reduced to a level where the Gaussian width of the IPS model can be constrained. For example, it is the small asymmetry in the UHRF ILS which allows us to constrain a symmetric IPS map, as we have chosen to use here. Nevertheless, this proves sufficient for measuring IPS variations in the MITLL3 chip using the assumptions above. As we demonstrate in Section 5, it may be possible to measure non-symmetric average IPS maps in future using additional information.

To summarize the above discussion, we may write our model of the IPS map for all pixels as a function of x (where we note that $x = 0$ is the middle of a pixel) as

$$\text{IPS}_i(x) = \text{IPS}(x) = B \exp\left(-x^2/2\sigma_{\text{IPS}}^2\right), \quad (7)$$

where the amplitude, B , is normalized such that $\int_{-1/2}^{1/2} \text{IPS}(x) dx = 1$. Here, σ_{IPS} , measured in units of pixels, is the IPS Gaussian width parameter which we measure. For example, $\sigma_{\text{IPS}} \gg 1$ pix indicates a flat average IPS map whereas $\sigma_{\text{IPS}} \lesssim 1$ pix indicates a strongly variable average IPS map.

Finally, note that the form of equation (6) is convenient because the integrand is the sum of a product of Gaussian functions, thereby allowing trivial numerical integration using the well-known Gamma function (e.g. Press et al. 1992).

4 AVERAGE INTRA-PIXEL SENSITIVITY MAP FROM A SINGLE COMB EXPOSURE

To measure the IPS variations using a single CCD exposure we assume that they are the same in all pixels and utilise the fact that each pixel (i.e. “copy” of the IPS map) is probed with a different flux distribution. By using a well-constrained model of the flux distribution across many pixels, σ_{IPS} – the Gaussian width of the average intrapixel sensitivity (IPS) map in our model – can be measured. From preliminary fits to ~ 200 -pixel sections of single CCD rows, it became clear that σ_{IPS} was covariant (i.e. somewhat degenerate) with several other parameters in our comb and instrumental line-shape models, e.g. σ_{ILS} , the width of the two Gaussian ILS components. Rather than attempt to fit many more pixels in a single CCD row, which may necessitate higher-order representations of the intensity

envelope function, $E(x)$, and comb function, $C(x)$, we instead utilized the full 2-dimensional (2D) comb information in our UHRF CCD exposures.

4.1 2D modelling of a single comb exposure

The example CCD exposure in Fig. 2 illustrates how the comb signal occupies more than 100 pixels in the spatial direction. That is, there are many “copies” of almost the same comb signal available for constraining σ_{IPS} . This means that, under our assumption that all CCD pixels have the same IPS variations, we can fit many CCD rows simultaneously by adding a very small number of additional free parameters to the model in equation (6).

Firstly, each of the terms of the comb function in equation (4) now becomes a function of CCD row, j . That is, the n th mode in row j can be written as

$$x_n^j = x_0(1 + a_1 j + a_2 j^2) + \omega_r n(1 + b_1 j) + \omega_2 n^2 \quad (8)$$

where we have now explicitly truncated the series at second order in n and limited the order in j in each term. Figure 2 clearly shows that the spatial direction of the spectrograph is tilted with respect to the CCD columns, i.e. $a_1 > 0$ to account for this tilt. But after exploring many 2D fits to various comb exposures and portions of the CCD, we found no evidence for distortions in this tilt, or for variations in the pixel-space repetition frequency with row. That is, both a_2 and b_1 were consistent with zero. Therefore, for all fits reported here we fixed a_2 and b_1 to zero.

Similarly, each of the parameters of the instrumental line-shape (ILS) could vary with j . By appropriately altering equation (5) to include polynomial dependence on j for all free parameters (e.g. σ_{ILS}), we explored various fits to search for evidence of this. However, we found no significant variations in the ILS in the spatial direction.

Finally, note that while the intensity envelope function, $E(x)$, clearly varies (slowly) with CCD row, j , it will not be strongly covariant with any IPS variations, the measurement of which is our main aim. Therefore, we simply allowed the parameters of $E(x)$ to be independently determined for each j .

4.2 Main results: limits on IPS variations from individual exposures

We searched for IPS variations in our 10 highest SNR (20-s long) exposures. In each exposure we concentrated on fitting a 50×320 pix (rows \times columns) region near the centre (highest SNR) of the comb signal. This represents about half the comb’s spatial extent and about 10 per cent of its spectral extent on the CCD. Preliminary fits showed that some portions of the fitted area were not well flat-fielded. From inspection of the raw images and the master flat-field frame, we determined that dust particles on the UHRF optics were most likely resulting in small flat-field residuals which varied slightly from exposure to exposure or at least between the comb and flat-field exposures. The portions of the fitted area were the same in the 10 exposures we studied in detail. Therefore, we simply masked these portions out of our χ^2 minimization analysis. We note in passing that 2D fits to different regions of the CCD did not reveal any obvious periodic CCD defects like those identified by Wilken et al. (2010).

Figure 4 shows part of a 2D fit to a representative exposure. In general, the fit is clearly a reasonable representation of the recorded

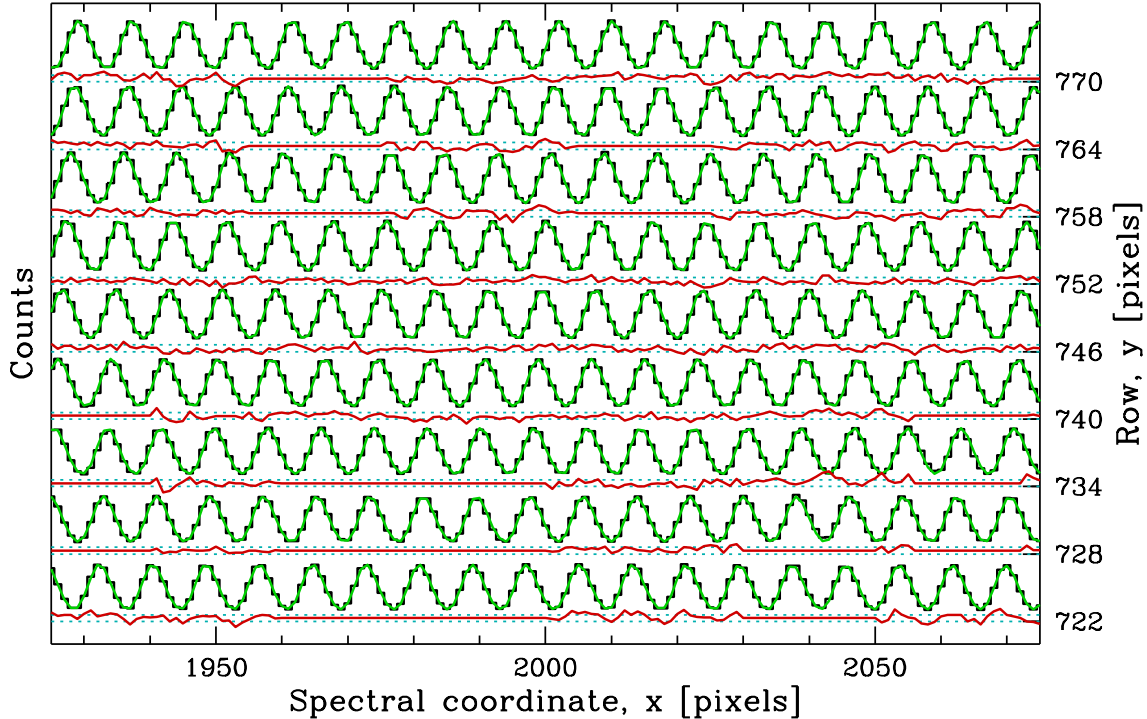


Figure 4. Part of a 2D fit to a single comb exposure. The flat-fielded spectra from every 6th fitted row are shown as black histograms overlaid by the model (green line) which was fitted to 50 rows and 320 pixels in the spectral direction. The normalized residuals are plotted below the spectrum of each row relative to the $\pm 3\text{-}\sigma$ levels (dotted blue lines). Note that some sections of residuals are all zero; these parts of the CCD have been masked due to problems with flat-fielding (see text). Note that the tilt of the spatial direction across the CCD columns is evident.

data. The χ^2 per degree of freedom, ν , was similar for all 10 exposures, $\chi^2_\nu \approx 2.9$ which, while not ≈ 1 , is not unreasonable, especially in the possible presence of additional, low-level flat-fielding errors. The residual spectra generally do not show coherent structures which repeat over ~ 8 pixel ranges, i.e. the transmitted comb mode spacing. Figure 4 clearly shows some exceptions to this general statement. However, we did not observe any obvious correlation between the positions of these exceptions in different exposures. They may very well result from IPS variations in small clusters of pixels, but we cannot quantitatively address that possibility with the data in hand. Again, we attempt here to constrain a model of the average IPS variations for the whole fitted area.

For all of the 10 individual exposures, simply including σ_{IPS} as a free parameter in the fit yielded best-fit values $\sigma_{\text{IPS}} > 2$ pix in all cases. This was independent of the starting guess for σ_{IPS} (and other parameters in the model), which was generally ~ 0.5 pix. In most cases σ_{IPS} grew from the starting guess value to 100 pix, the arbitrary limit imposed in our code. And in all cases, the best fit value was entirely consistent with $\sigma_{\text{IPS}} = \infty$. That is, under the assumptions of our IPS model, we do not detect significant average IPS variations.

To ensure that our χ^2 minimization code was functioning correctly we fitted simulated versions of the 10 comb spectra. The real comb flux was replaced with the best-fit model (without IPS variations) with Gaussian noise added which was derived using the real flux error estimates. The synthetic realisations were fitted in the same way, and with the same free parameters, as the real spectra. Figure 5 illustrates one aspect of the comparison between the results from one comb exposure and the average results from 25 simulated versions of it. By holding σ_{IPS} fixed at certain values and plotting the deviation in χ^2 from its minimum, $\Delta\chi^2$, we gain a more

accurate understanding of the minimum value of σ_{IPS} allowed for each exposure. Because χ^2_ν is not close to unity for the real exposures, but it is (by construction) for the simulations, we can test the veracity of the usual assumption that confidence intervals for σ_{IPS} may be derived after normalizing χ^2 by $(\chi^2_{\nu,\text{min}})^{1/2}$, the square root of the minimum χ^2_ν . Under this normalization, Fig. 5 shows very similar results for the real and simulated spectra.

For the particular exposure studied in Fig. 5 we can rule out $\sigma_{\text{IPS}} < 1.0$ pix (< 0.5 pix) at the 68 per cent (95 per cent) significance level. These constraints on σ_{IPS} were uniformly replicated for the same fitted region across the 10 exposures we studied in detail. By co-adding the plots of $\Delta\chi^2/(\chi^2_{\nu,\text{min}})^{1/2}$ versus σ_{IPS} for all 10 exposures, and recalling that we fitted the same region of the CCD in all cases, we form a joint constraint on the Gaussian width of our assumed IPS variation map: $\sigma_{\text{IPS}} > 1.2$ pix at 99.7 per cent ($3\text{-}\sigma$) confidence. This value of σ_{IPS} corresponds to variations in the IPS across the spectral direction of the pixel of < 8 per cent.

Instead of a decrease in the IPS from the pixel centre to its edges, we also explored an IPS map with a minimum at the pixel centre by adding unity to equation (7) and allowing $B < 1$. We find very similar results to those above: σ_{IPS} is constrained to be > 1.3 pix at 99.7 per cent confidence. That is, we rule out IPS variations of > 7 per cent at $3\text{-}\sigma$ significance under the assumptions of our modified (up-side down Gaussian) model.

Finally, to demonstrate that detecting non-zero IPS variations is possible using our χ^2 minimization technique (under the assumptions of our 2D modelling), we again fit simulated versions of the real comb spectra, this time with finite values of σ_{IPS} . The SNR of the simulated spectra again matched the corresponding real spectra. In all simulations the best-fit value of σ_{IPS} broadly matched the input value. This was simple to assess for input values $\sigma_{\text{IPS}} \lesssim 1.5$ pix

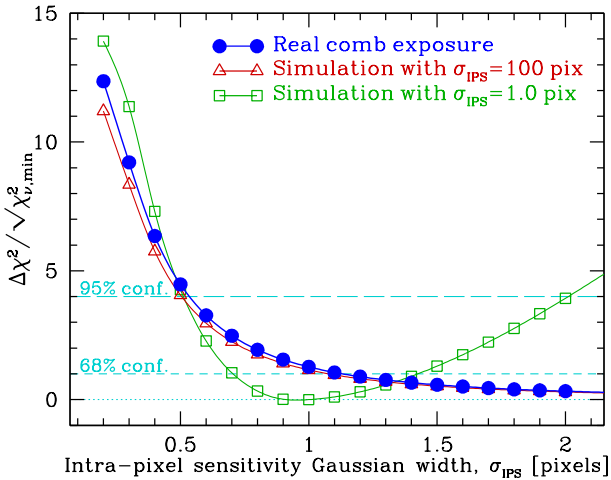


Figure 5. Results from 2D fit to the central part (50×320 pixels) of a single flat-fielded comb exposure. The plot represents the increase in χ^2 from its minimum value, χ_{\min}^2 (i.e. $\Delta\chi^2 \equiv \chi^2 - \chi_{\min}^2$) as a function of the Gaussian width of the intra-pixel sensitivity (IPS) variations, σ_{IPS} . $\Delta\chi^2$ is normalized by $\sqrt{\chi_{\min}^2}$ where χ_{\min}^2 is the minimum value of χ^2 per degree of freedom, χ_{ν}^2 , so that confidence intervals can be calculated directly from the plot. σ_{IPS} is unbounded above in the fit to the real comb exposure (blue curve with circular points). That is, we cannot rule out the null hypothesis of zero average IPS variations in that exposure. However, $\sigma_{\text{IPS}} \lesssim 0.5$ pix is ruled out at 95 per cent confidence ($\Delta\chi^2 / \sqrt{\chi_{\min}^2} \approx 4$). A fit to a simulated version of the same comb exposure with a flat IPS map inserted yield very similar results (red curve with triangular points). The green curve with square points shows the results from a fit to the same simulation in which a non-flat IPS map was used, i.e. $\sigma_{\text{IPS}} = 1$ pix. The definite minimum demonstrates that non-flat IPS variations could have been detected given the assumptions in our model of the comb exposures.

but judging formal statistical consistency between the input and best-fit values was more difficult when σ_{IPS} was larger. The ultimate reason for this is that the IPS map is very flat for large σ_{IPS} . This is illustrated in Fig. 5 which shows the variation in χ^2 with fixed fitted values of σ_{IPS} for a single realisation with an input $\sigma_{\text{IPS}} = 1$. In this example there is a clear minimum in χ^2 near the input value of σ_{IPS} . However, it is also clear that χ^2 's sensitivity to σ_{IPS} diminishes with increasing σ_{IPS} , i.e. the χ^2 curve is not parabolic at $\sigma_{\text{IPS}} \gtrsim 1$. Thus, the formal statistical error on σ_{IPS} derived from the covariance matrix in our χ^2 minimization scheme will not be reliable for large σ_{IPS} . This problem clearly also applies to the constraints on σ_{IPS} derived from our real comb exposures above. This is the reason we used the χ^2 curve for the fit to each exposure, rather than the formal error from the covariance matrix, to derive confidence limits on any IPS variations.

To summarize the results above, we have demonstrated that any symmetric component of the average intra-pixel sensitivity (IPS) variations can be detected in a single LFC exposure provided that many hundreds of pixels can be modelled simultaneously. The AAT/MITLL3 chip's average IPS map deviates from being flat by < 8 per cent in a symmetric manner about the pixel centre in the direction along CCD rows. However, under our model assumptions, we cannot measure or rule out a significant asymmetric component to the average IPS map. For example, the IPS map may slope from one side of the pixel to the other, but we cannot detect this by modelling a single exposure. The simple reason for this is that such a slope is closely degenerate with the measured position of the comb

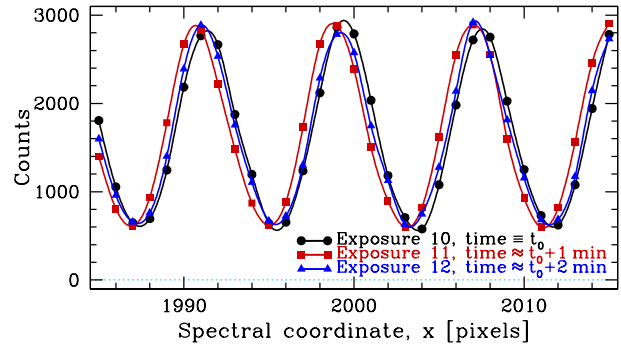


Figure 6. Shifts between comb spectra on short time-scales. Plotted are small sections of a single row of three 1-s long flat-fielded comb spectra (traced by spline curves to between distinguish them). The exposures were taken approximately 1 min apart and all three had the same repetition frequency (f_{rep}) and carrier envelope offset frequency (f_{CEO}), yet they show clear, stochastic shifts of ~ 0.4 pixels.

with respect to the CCD pixel grid. We return to this point in Section 5.2. In the next Section we discuss how a series of offset comb exposures might allow that degeneracy to be removed.

5 INTRA-PIXEL SENSITIVITY MAP FROM A SERIES OF OFFSET COMB EXPOSURES

5.1 Observed series

With a view to detecting any very small average IPS variations, the 10×20-s comb exposures with high SNR utilized in the previous section were taken in series with small offsets in the LFC signal applied between exposures. The offsets were generated by slightly altering the repetition frequency of the mode-locked laser, f_{rep} , which was observed to be stable between exposures. The offset in f_{rep} between each exposure was ~ 15 Hz so that the comb modes at 780 nm would shift by ~ 50 m s $^{-1}$, or 0.5 spectral pixels. The carrier-envelope offset frequency, f_{CEO} , was also monitored and fluctuations were negligible (< 10 m s $^{-1}$) during the series of exposures.

However, upon inspecting the series of offset comb exposures, it was apparent that the observed shifts in the comb modes did not accurately reflect those expected from the offsets applied to f_{rep} between successive exposures. To investigate this we took another series of 10 short (1-s) exposures with no offsets in f_{rep} applied between them. That is, including the CCD read-out time of each exposure, a 1-s exposure was taken approximately every minute and, since neither f_{rep} nor f_{CEO} changed appreciably during the 10 min series, we expected no shifts between the comb modes. However, we discovered fairly large stochastic shifts between successive comb exposures. These were typically ≤ 0.2 pixels but some were as large as ~ 0.4 pixels. An example from 3 successive 1-s exposures is shown in Fig. 6. Furthermore, no two successive exposures had zero shift between them, indicating that the time-scale for these shifts is substantially less than 1 min.

The origin of these shifts is not clear from our comb spectra, but the fast time-scale suggests that a purely thermal drift within UHRF is an unlikely culprit and that a more likely explanation is small mechanical oscillations or jumps/relaxations in the spectrograph. UHRF's main components and camera are mounted on a large (~ 3 -m), vibration-damped and isolated bench. The slit assembly is mounted on the same bench. However, the pre-slit area upon

which our LFC launch setup was mounted (see Fig. 1) is, at least in principle, decoupled from the spectrograph bench. Thus, oscillations induced by moving components in the pre-slit area (e.g. the rotating diffuser) should not cause the slit itself to oscillate. However, it remains possible the other equipment in the pre-slit area might transmit some vibrations to the slit assembly, which may have been responsible for the short time-scale, stochastic shifts we observe. If such oscillations/vibrations did not originate from our equipment, they may also affect astronomical observations with UHRF; however, they are unlikely to have been detectable in UHRF before because of the much longer ThAr exposure times required (i.e. several minutes). Observations with the University College London Echelle Spectrograph, UCLES, which uses the same coude room and slit assembly as UHRF, might also be affected. We would be interested to learn whether users of UCLES have identified such problems before, but to our knowledge they have not been reported in the literature.

Unfortunately, these stochastic shifts between exposures mean that we cannot reliably model the observed series of offset comb exposures to constrain IPS variations. One should consider whether the analysis of the individual 20-s exposures in Section 4 was affected by this instability. The effect of quickly varying shifts in the comb position, averaged over a comparably long exposure, should be to increase the observed comb mode width, or σ_{ILS} as parametrized in our comb models. We do not observe a larger σ_{ILS} for the 10×20 -s comb exposures compared to the 10×1 -s ones: $\langle \sigma_{\text{ILS}} \rangle = 1.632$ compared to $\langle \sigma_{\text{ILS}} \rangle = 1.629$ pix, respectively. However, the root-mean-square (RMS) variations in these quantities – 0.006 and 0.011 pix, respectively – may be too large to detect the increase in width expected: if random comb shifts have RMS ~ 0.2 pix then σ_{ILS} would broaden by just ~ 0.01 pix. Even if this effect were present in the 20-s comb exposures, our model of the comb flux across the CCD pixels is still likely to be adequate and so the constraints on IPS variations we derive are unlikely to be strongly affected.

5.2 Simulated series

While the short time-scale instabilities in UHRF prevent us from constraining the average IPS variations using a real series of offset comb exposures, we can nevertheless demonstrate this possibility using simulated comb spectra. We simulated 10 spectra, each with a single CCD row 320 pixels long. The comb signal was generated using the best-fitting parameters derived from row 750 of the CCD exposure studied in Section 4.2 (see Figs. 2 & 3), including the double-Gaussian instrumental line-shape. Gaussian random noise was added to each spectrum independently, with the average SNR set to the same value as in the real CCD exposure. However, we introduced 0.8-pixel offsets between the comb functions for successive spectra. We then simultaneously fitted comb functions to all 10 spectra, the key assumption being that the relative offsets between spectra were known; if the LFC system is absolutely calibrated then this will be true to very high precision.

Figure 7 shows the results of the fits to the simulated spectra. Similar to the simulations in the previous section, the input IPS model was a Gaussian with $\sigma_{\text{IPS}} = 0.4$ pix centred at $x = 0$. That is, the Gaussian was centred at the middle of the pixel and σ_{IPS} was a free parameter. Note that the ILS and envelope function parameters were also free in this fit. Figure 7 shows that this symmetric IPS model is recovered with a relatively small uncertainty in σ_{IPS} of 0.03 pix. This demonstrates that a series of offset comb spectra can

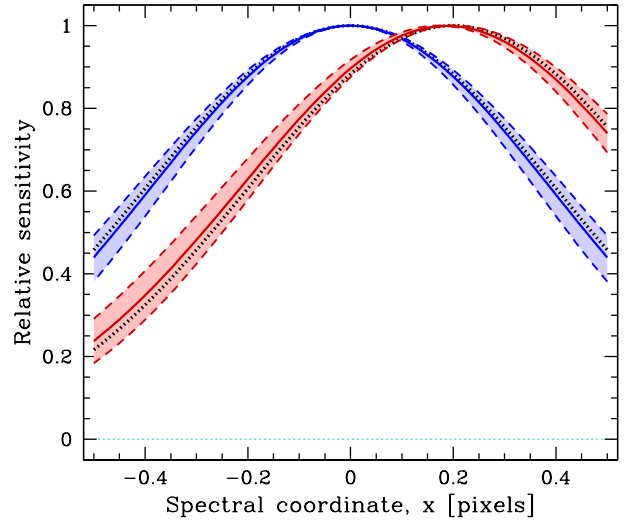


Figure 7. Recovery of average intra-pixel sensitivity (IPS) map from series of offset comb spectra. Ten single-row, 320-pixel comb spectra were simulated with the same parameters (similar to those of our real comb exposures), but with offsets of 0.8 pixels between their respective comb functions and different noise realisations. The blue (symmetric about $x = 0$) shaded region shows the $1\text{-}\sigma$ uncertainty range in the measured IPS map (solid curve) when only the Gaussian width of the IPS model is a fitted free parameter. The red (asymmetric) region and curves represent the results when both the Gaussian IPS width and its position along x are free parameters and where it is assumed that the absolute position of the comb with respect to the CCD pixel grid is known. In both cases the input IPS model is shown as a black dotted curve.

be used to characterise the symmetric component of the average IPS map.

The main reason a series of offset spectra can strongly constrain the IPS variations, even with fairly few pixels (e.g. a single CCD row) assumed to have the same IPS map, is that the comb flux distribution across each pixel is changed by a known amount when the comb is offset by a known amount. However, as with the 2D analysis of a single exposure in Section 4, any asymmetric component of the IPS map is highly degenerate with the overall position of the comb. That is, without knowing where the comb modes fall with respect to the CCD pixel grid, asymmetries in the average IPS map cannot be reliably determined. If some additional information could be gained about where the comb light is striking pixels, perhaps by adjusting a physical mask in front of the CCD, then the same fitting technique could be used to recover asymmetries in the IPS map.

As an example of this, we simulated another ten 320-pixel, single-row comb spectra in the same way as above but with an asymmetric input IPS map, i.e. a Gaussian, as before, but shifted with respect to the pixel centre. It was then assumed that the absolute position of the comb modes with respect to the pixel grid was known. Figure 7 shows that the fitting technique indeed recovers the asymmetry in the input IPS model with high accuracy. Much higher precision measurements of the average IPS variations should be possible if the instrumental line-shape (ILS) is also known accurately *a priori* (or measured independently) and not simultaneously constrained by the comb spectra. With a large enough number of high-SNR exposures with very small, known offsets, and with known comb-mode–CCD-grid positioning and ILS information, it should be possible to measure the IPS map of every illuminated CCD pixel.

6 SUMMARY

We reported the successful test of a laser frequency comb (LFC) system on the Ultra High Resolution Facility (UHRF) spectrograph at the Anglo-Australian Telescope (AAT). Figure 1 shows the experimental setup used. The high spectral resolution of UHRF ($R \approx 940000$) allowed a commercial fibre laser with a fairly typical repetition frequency (f_{rep}) to be used.

A Fabry-Perot cavity was used to widen the effective separation between modes to $\sim 1\text{GHz}$ (by suppressing 10 of every 11 modes) so they could be resolved apart by UHRF. The LFC spectra were recorded with the ‘MITLL3’ CCD chip at $\approx 780\text{nm}$ in a single echelle order of UHRF covering $\approx 10\text{\AA}$. An example exposure is shown in Fig. 2.

Our main goal in the LFC test was to demonstrate that LFC spectra could be used to characterize the average intra-pixel sensitivity (IPS) map of astronomical CCDs *in situ*. This meant that actively self-calibrating the LFC (i.e. controlling f_{rep} and f_{CEO} , not just measuring/monitoring them) was not necessary, which minimized the equipment required on-site.

We demonstrated the measurement of IPS variations using a single comb exposure by modelling the comb flux in 50×320 pixels in the spatial and spectral directions, respectively – see Figs. 4 & 5. For a simple Gaussian model of the average IPS variations where the sensitivity falls off symmetrically about the pixel centre, the IPS map of the AAT/MITLL3 chip deviates from flat by < 8 per cent. A similar constraint on an inverted map (i.e. sensitivity increasing towards the pixel edges) was also obtained.

The instrumental line-shape (ILS) was also modelled in this process, and we found that a double-Gaussian ILS was sufficient to fit our comb spectra – see Fig. 3. This ILS is very similar to that found when commissioning UHRF (Diego et al. 1995).

By slightly adjusting the repetition frequency between comb exposures (by changing the length of the fibre laser’s free-space section), we obtained a series of exposures with known offsets between their respective comb signals along the spectral direction of the CCD. In this way we intended to more strongly constrain the IPS variations in a single CCD row. However, a series of shorter exposures *without* offsets between them revealed short time-scale ($\lesssim 1\text{min}$) random shifts between exposures of up to ≈ 0.4 pixels (or $\approx 40\text{ms}^{-1}$) – see Fig. 6. This precludes a thorough analysis of the series of offset comb exposures for constraining IPS variations. Nevertheless, we used simulated spectra whose parameters closely matched our real spectra to demonstrate that, with a stable spectrograph, such a series of comb exposures should allow symmetric departures from a flat average IPS map of a single CCD row (320 pixels) to be strongly constrained – see Fig. 7.

Despite demonstrating that the *symmetric* component of average IPS variations can be constrained using LFCs, it is clear that, without knowing *a priori* where the comb modes fall with respect to the CCD grid, any *asymmetric* component of the IPS map cannot be reliably measured. This could be an important aspect of IPS variations to measure for some applications, especially those where long-term, effectively absolute calibration is required (e.g. the real-time observation of the drift in Lyman- α forest lines in quasar spectra). In future, perhaps the relationship between the physical position of the comb modes and the CCD grid might be established through some kind of physical CCD masking procedure, or by ‘switching off’ some CCD pixels and obtaining a series of offset comb exposures. Exploring such possibilities may be required to fully realise absolute wavelength calibration using CCDs in astronomy.

ACKNOWLEDGMENTS

We are indebted to the truly exceptional staff at the Australian Astronomical Observatory for enabling the experiment reported here. In particular, the expertise and resourcefulness of Stuart Barnes, Steve Lee, Rob Dean, Stephen Marsden, Doug Gray, Steve Chapman, John Collins and Winston Campbell ensured its success. MTM thanks the Australian Research Council for a QEII Research Fellowship (DP0877998), while AL, CL and PL thank it for supporting this work under DP0877938.

REFERENCES

- Bahcall J.N., Sargent W. L.W., Schmidt M., 1967, ApJ, 149, L11
 Benabid F., Biancalana F., Light P.S., Couny F., Luiten A., Roberts P.J., Peng J., Sokolov A.V., 2008, Opt. Lett., 33, 2680
 Benedict A.J. et al., 2010, Opt. Express, 18, 19175
 Cundiff S.T., Ye J., 2003, Rev. Mod. Phys., 75, 325
 Dekker H., D’Odorico S., Kaufer A., Delabre B., Kotzlowski H., 2000, Proc. SPIE Vol. 4008, 4008, 534
 Diego F. et al., 1995, MNRAS, 272, 323
 Fisher R.A., 1958, Statistical methods for research workers. Harper, New York
 Ivanchik A., Petitjean P., Varshalovich D., Aracil B., Srianand R., Chand H., Ledoux C., Boissé P., 2005, A&A, 440, 45
 Jones D.J., Diddams S.A., Ranka J.K., Stentz A., Windeler R.S., Hall J.L., Cundiff S.T., 2000, Sci, 288, 635
 King J.A., Murphy M.T., Ubachs W., Webb J.K., 2011, MNRAS, 417, 3010
 Liske J. et al., 2008, MNRAS, 386, 1192
 Locke C.R., Ivanov E.N., Light P.S., Benabid F., Luiten A.N., 2009, Opt. Express, 17, 5897
 Loeb A., 1998, ApJL, 499, L111
 Lovis C. et al., 2006, Nat, 441, 305
 Ma L.-S. et al., 2004, Sci, 303, 1843
 Malec A.L. et al., 2010, MNRAS, 403, 1541
 Marcy G.W., Butler R.P., 1996, ApJL, 464, L147
 Mayor M., Queloz D., 1995, Nat, 378, 355
 Murphy M.T. et al., 2007, MNRAS, 380, 839
 Murphy M.T., Webb J.K., Flambaum V.V., 2003, MNRAS, 345, 609
 Pasquini L. et al., 2006, in IAU Symp.Ser., Vol. 232, Scientific Requirements for Extremely Large Telescopes, Whitelock P., Dennefeld M., Leibundgut B., eds., Cambridge Univ.Press, Cambridge, UK, pp. 193–197
 Press W.H., Teukolsky S.A., Vetterling W.T., Flannery B.P., 1992, Numerical recipes in C. The art of scientific computing. Cambridge University Press, UK
 Reichert J., Holzwarth R., Udem T., Hänsch T.W., 1999, OptCo, 172, 59
 Sandage A., 1962, ApJ, 136, 319
 Schmidt P.O., Kimeswenger S., Kaeuffl H.U., 2008, in The 2007 ESO Instrument Calibration Workshop, Kaufer A., Kerber F., eds., ESO Astrophysics Symposia series, Springer-Verlag, Berlin Heidelberg, Germany, pp. 409–414
 Steinmetz T. et al., 2008, Sci, 321, 1335
 Tinney C.G., Butler R.P., Marcy G.W., Jones H. R.A., Penny A.J., McCarthy C., Carter B.D., Bond J., 2003, ApJ, 587, 423
 Toyozumi H., Ashley M. C.B., 2005, PASA, 22, 257
 Udem T., Holzwarth R., Hänsch T.W., 2002, Nat, 416, 233
 Varshalovich D.A., Levshakov S.A., 1993, JETP Lett., 58, 237
 Webb J.K., Flambaum V.V., Churchill C.W., Drinkwater M.J., Barrow J.D., 1999, Phys. Rev. Lett., 82, 884
 Webb J.K., King J.A., Murphy M.T., Flambaum V.V., Carswell R.F., Bainbridge M.B., 2011, Phys. Rev. Lett., 107, 191101
 Wilken T. et al., 2010, MNRAS, 405, L16

This paper has been typeset from a $\text{\TeX}/\text{\LaTeX}$ file prepared by the author.